

Shear Localization–Martensitic Transformation Interactions in Fe-Cr-Ni Monocrystal

M.A. MEYERS, B.Y. CAO, V.F. NESTERENKO, D.J. BENSON, and Y.B. XU

A Fe-15 wt pct Cr-15 wt pct Ni alloy monocrystal was deformed dynamically (strain rate $\sim 10^4 \text{ s}^{-1}$) by the collapse of an explosively driven thick-walled cylinder under prescribed initial temperature and strain conditions. The experiments were carried out under the following conditions: (a) alloy in austenitic state, temperature above transformation temperature; (b) alloy in transformed state; and (c) alloy at temperature slightly above M_s , propitiating concurrent shear-band propagation and martensitic transformation. The alloy exhibited profuse shear-band formation, which was a sensitive function of the deformation condition. Stress-assisted and strain-induced martensitic transformation competes with shear localization. The alloy deformed at a temperature slightly above M_s shows a significantly reduced number of shear bands. The anisotropy of plastic deformation determines the evolution of strains and distribution of shear bands. The different conditions showed significant differences that are interpreted in terms of the microstructural anisotropy. Calculated shear-band spacings based on the Grady–Kipp (GK) and Wright–Ockendon (WO) theories are compared with the observed values. The microstructure within the shear bands was characterized by transmission electron microscopy. Regions of sub-micron grain sizes exhibiting evidence of recrystallization were observed, as well as amorphous regions possibly resulting from melting and rapid resolidification.

I. INTRODUCTION

METALS deform plastically by dislocation glide (slip), mechanical twinning, or martensitic transformations. This plastic deformation exhibits in many cases inhomogeneities due to microstructural effects. Shear localization is an extreme case of inhomogeneous deformation when plastic deformation localizes on a thin region of a specimen. Shear localization is very important because it is often a precursor to failure. In most cases, shear localization is associated with a local softening of the structure. This softening can be due to thermal or geometrical reasons. In geometrical softening, the structure orients itself to a direction that is easier (*i.e.*, requires less stress) for glide. The rotation of crystallographic slip planes in response to straining in ductile crystalline solids is an example.^[1] However, shear localization is not restricted to crystalline solids; metallic glasses and partially crystalline polymers are prone to shear localization. Granular and fragmented ceramics also undergo localization.^[2–6] For these cases, thermal softening is replaced by structural softening such as particle breakdown. The brittle material may undergo a comminution process in a narrow region, leading to softening. In special cases, localization has been predicted to occur even during hardening (Rudnicki and Rice^[7]).

In thermal softening, the local increase in temperature can result in a softening that leads to localization. In the extreme case in which the strain rate is so high that the local heat generated cannot escape from the deformation area, these bands are called adiabatic shear bands. Regardless of the initial softening mechanism, the localized deformation leads to an acceleration of strain rate. Eventually, there are heat concentration and thermal effects in most situations. There are several excellent reviews available in the literature. Review articles by Rogers,^[8] and the proceedings of a 1992 symposium on shear instabilities (Armstrong *et al.*^[9]), contain a significant amount of information. The reader is also referred to the books by Bai and Dodd,^[10] Meyers,^[11] and Wright.^[12]

Nesterenko *et al.*^[5,13–15] have established that shear bands in metals self-organize with a characteristic spacing that is a function of material parameters; it was found that this spacing evolves with the length of the shear bands, so that shorter shear bands have a smaller spacing.

All previous research on shear localization in metals has involved dislocation glide (slip) or mechanical twinning as the plastic deformation mechanism. The research whose results are presented herein had as its purpose the determination, if any, of the interaction between shear localization and martensitic transformation.

II. MATERIAL AND EXPERIMENTAL METHODS

The alloy Fe-15 wt pct Cr-15 wt pct Ni was chosen for this investigation because it has a very well characterized deformation and transformation response. A monocrystalline cylindrical specimen with 32-mm diameter was grown at the Advanced Research and Development Laboratory at Pratt and Whitney Aircraft (West Palm Beach, FL). This alloy was homogenized at 1500 K for 72 hours and has an fcc structure. Figure 1 shows the estimated M_s temperature for this alloy,

M.A. MEYERS, V.F. NESTERENKO, and D.J. BENSON, Professors, and B.Y. CAO, Graduate Student, are with the Department of Mechanical and Aerospace Engineering, University of California, San Diego, La Jolla, CA 92093-0411. Contact e-mail: mameyers@ucsd.edu or bucao@ucsd.edu. Y.B. XU, Professor, is with the Institute of Metal Research, Chinese Academy of Sciences, Shenyang 110016, People's Republic of China.

This article is based on a presentation given in the symposium "Dynamic Deformation: Constitutive Modeling, Grain Size, and Other Effects: In Honor of Prof. Ronald W. Armstrong," March 2–6, 2003, at the 2003 TMS/ASM Annual Meeting, San Diego, California, under the auspices of the TMS/ASM Joint Mechanical Behavior of Materials Committee.

Table I. Material Parameters for the Shear-Band Spacing Calculation^[23]

Density ρ (g/cm ³)	Heat Capacity C (J/Kg K)	Thermal Conductivity k (W/mK)	Thermal Softening Factor a (K ⁻¹)	Strain Rate Hardening Index m
8.7	500	14.7	7.2×10^{-4}	0.026
Strain-Hardening Index n	Shear Stress (MPa)	Dynamic Shear Stress (MPa)	Shear Strain Rate $\dot{\gamma}$ (s ⁻¹)	
0.09 for [100]	150	285	6×10^4	
0.03 for [110]				

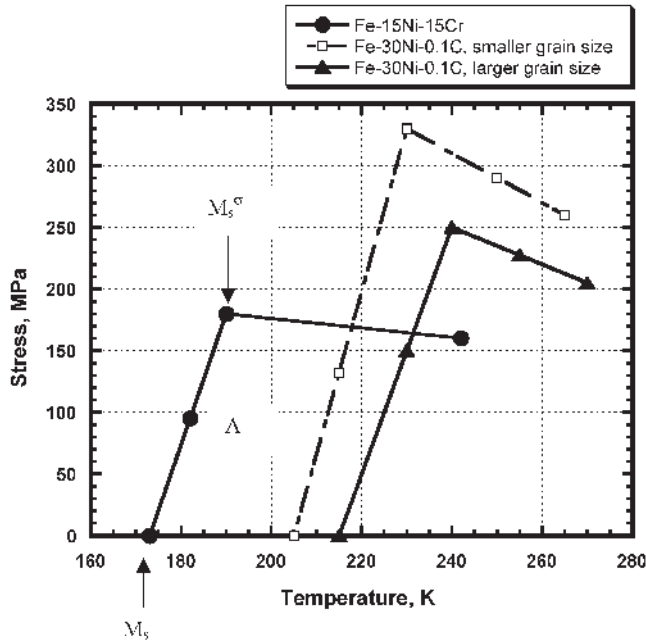


Fig. 1—Temperature dependence of the material yield strength for Fe-15Cr-15Ni: Fe-15Cr-15Ni, $M_s = 173$ K (data from • Stone and Thomas^[16] and ▲, □ Guimaraes *et al.*^[17]); $D = 0.211$ and 0.101 mm.

obtained by using point A (182 K, 80 MPa^[16]) and the assumed slope of the stress-assisted range. For comparison, the measured results for Fe-30 wt pct Ni-1 wt pct C^[17] with two grain sizes are shown in the same plot. As expected, the reduction of grain size affects the M_s temperature.

Patel and Cohen^[18] established the effect of applied stress on M_s . They did this both analytically and experimentally. This was carried out by computing the energy of interaction, U_s , between the applied stress, and the transformation strains, $\gamma_0 = 0.2$ (shear) and $\epsilon_0 = 0.04$ (dilatational):

$$U_s = \tau\gamma_0 + \sigma\epsilon_0 \quad [1]$$

where τ is the shear stress along the habit plane in the shear direction and σ is the stress normal to the habit plane. More complex and elaborate formulations have been developed by Eshelby^[19,20] and Mura^[21] but this simple equation suffices for the purpose of this calculation. From Eq. [1], we can obtain

$$U_s = \frac{1}{2}\gamma_0|\sigma| \sin 2\theta + \frac{1}{2}\epsilon_0|\sigma|(1 + \cos 2\theta) \quad [2]$$

where θ is the angle between the external stress direction and the normal to the habit plane.

The angle at which this interaction energy is maximized is obtained by differentiating Eq. [2] respect to θ :

$$\frac{dU_s}{d\theta} = \gamma_0|\sigma| \cos 2\theta + \epsilon_0|\sigma|(-\sin 2\theta) \quad [3]$$

This corresponds to $\theta = 39.35$ deg.

The effect of the stress is expressed by

$$\frac{U_s}{\sigma} = \frac{dU_s}{d\sigma} = \frac{1}{2}\gamma_0 \sin 2\theta + \frac{1}{2}\epsilon_0(1 + \cos 2\theta) \quad [4]$$

The two solutions are

$$\frac{dU_s}{d\sigma} = 0.122 \quad \text{for tensile stresses} \quad [5]$$

$$\frac{dU_s}{d\sigma} = 0.068 \quad \text{for compressive stresses} \quad [6]$$

The molar volume of the Fe-15 wt pct Ni-15 wt pct Cr alloy is $M = 7.09 \times 10^{-6}$ m³/mole. The effect of temperature on the driving energy for martensitic transformation, $\Delta F^{\alpha' \rightarrow \gamma}$, is usually assumed to be linear (*e.g.*, Kaufman and Cohen^[22]).

This temperature dependency, for a Fe-30 wt pct Ni alloy, is given by (Figure 3.11^[22]):

$$\frac{d\Delta F^{\alpha' \rightarrow \gamma}}{dT} = 6.97 \text{ J/mole} \cdot \text{K} \quad [7]$$

The subsequent product provides the effect of stress on M_s . This M_s , triggered by stress, is called M_s^σ .

$$\frac{dU_s}{d\sigma} \times \frac{dT}{d\Delta F^{\alpha' \rightarrow \gamma}} \times M = \frac{dM_s^\sigma}{d\sigma} \quad [8]$$

Using the values from Eqs. [5] and [6], we obtain, for tensile stresses,

$$\frac{dM_s^\sigma}{d\sigma} = 0.124 \text{ K/MPa} \quad [9]$$

$$\frac{dM_s^\sigma}{d\sigma} = 0.069 \text{ K/MPa} \quad [10]$$

Thus, the preceding calculations provide a theoretical explanation for the change in M_s with applied stress. These results are shown in Figure 1 for Fe-15Cr-15Ni. For comparison

purposes, experimental results by Guimarães *et al.*,^[17] are also given. The inverse slopes of the M_s^σ dominated region are on the order of 0.1 K/MPa, in agreement with Eq. [9].

Although Stone and Thomas^[16] do not report an M_s for this alloy, it is estimated to be equal to 177 K. The term M_s^σ , the highest temperature at which stress-assisted martensite can be formed, is estimated to be 190 K. In order to establish the interaction between shear bands and martensite transformation, three regions of mechanical response were chosen:

- $T < M_s$: alloy in martensitic state;
- $M_s < T < M_s^\sigma$: concurrent deformation and transformation; and
- $T > M_s^\sigma$: no transformation.

The dynamic method of plastic deformation used in this investigation, the collapsing thick-walled cylinder, has been

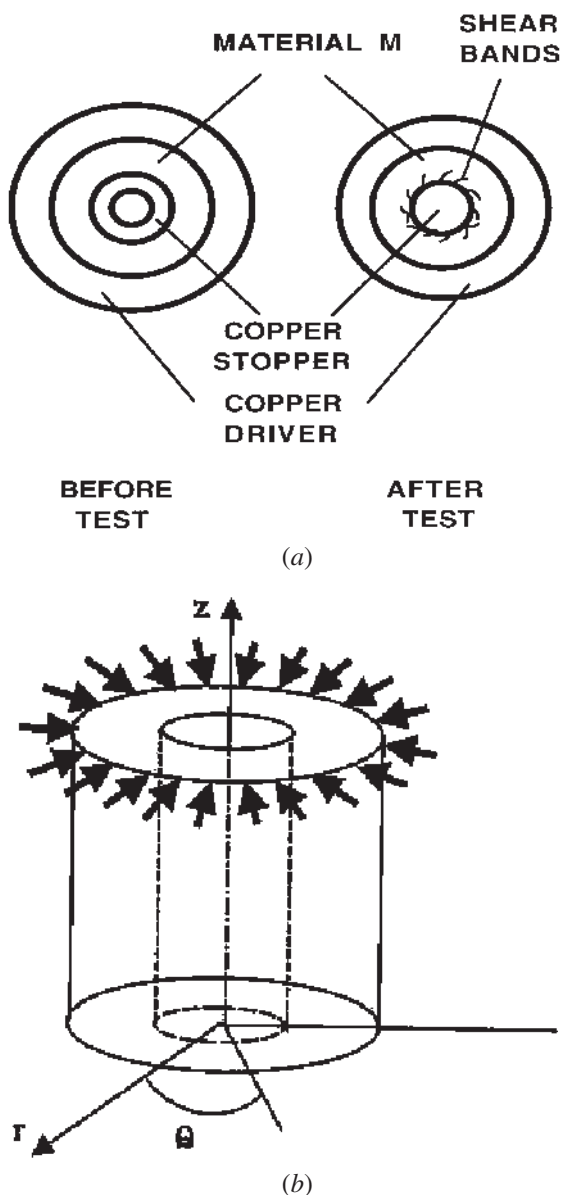


Fig. 2—Experimental method, thick-walled cylinder test: (a) cross sections and (b) overall view with explosive energy marked by arrows.

used and thoroughly characterized for multiple shear-band generation.^[23] The thick-walled cylinder implosion technique was introduced by Nesterenko^[6] and Nesterenko and Bondar^[24] and represents an improvement from the confined exploding cylinder technique developed in SRI (SRI International).^[25] The technique is described in detail elsewhere^[6,15,24,26] and will be only briefly presented here.

The specimen is sandwiched between a copper driver tube and a copper stopper tube and is collapsed inward during the test. Figure 2(a) shows the initial and imploded configurations. Oxygen free high conductivity (OFHC) copper was used to make these tubes. The internal diameters of the inner copper tube were selected to produce prescribed and controlled final strains. In some special cases, a central steel rod was also used. The explosive is axi-symmetrically placed around the specimen (Figure 2(b)). The detonation is initiated on the top. The expansion of the detonation products exerts a uniform pressure on the cylindrical specimen and drives the specimen to collapse inward. The detonation velocity of the selected explosive is approximately 4000 m/s and its density is 1 g/cm³. The velocity of the inner wall of the tube was determined by an electromagnetic gage.^[27] The dimensions and experimental assembly are shown in Figure 3. The samples had internal diameter 14 mm, external diameter 21 mm, and height 30 mm. They were shrink fitted in the thick-walled cylinder geometry between a copper stopper tube (with inner and outer diameters 12.5 and 14 mm, respectively) and copper driver tube with diameters 21 and 31 mm, respectively. This geometry provides an effective strain equal to 0.92 in the internal surface of collapsed sample. Samples were supported at the top and bottom by copper tubes with height 30 mm and similar diameters (Figure 3). The diameter of the explosive charge (ammonite 6JV) was 61 mm. For

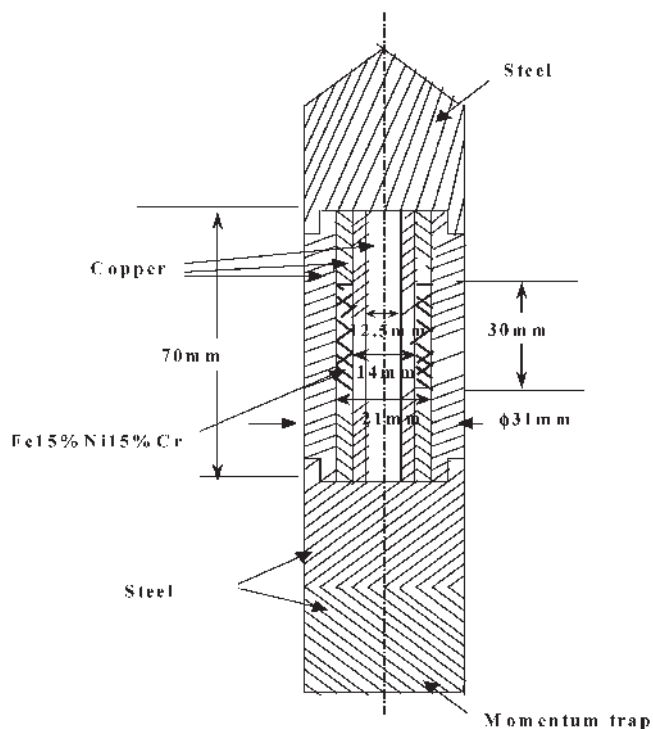


Fig. 3—Dimensions of experimental setup.

experiments at low temperatures, the explosive charge was placed around a steel tube with internal diameter 31 mm and wall thickness 1 mm.

The experimental conditions for the three experiments were as follows.

1. $T < M_s$: alloy in martensitic state; test was conducted at 190 K. The sample was first cooled to the 77 K and transformed. After that, the temperature measured was raised to 190 K, when explosive charge was detonated.
2. $M_s < T < M_s^\sigma$: concurrent deformation and transformation. Experiment conducted at 188 K (-85°C). The sample was cooled by immersion in liquid isopropanol ($\text{CH}_3\text{CH}(\text{OH})\text{CH}_3$) inside the steel container. The container was placed into liquid nitrogen and kept there until freezing at -89.5°C . Then, the sample was rapidly removed from isopropanol and placed into a thick-wall cylinder assembly. The initiation of the explosive charge was performed 1.2 minutes after that.
3. $T > M_s^\sigma$: no transformation. Experiment was conducted at 273 K.

The initial velocity of collapse of the inner tube was found by Nesterenko *et al.*^[27] to be approximately 200 m/s. It is possible to obtain an estimate of the upper bound of this velocity by a simple analytical calculation, which equates the chemical energy of the explosive to the kinetic energy of the collapsing cylinder and of the detonation gases. This is the Gurney approach. An equation applicable to the geometry used here was developed by Meyers and Wang.^[28] Neglecting the effect of plastic deformation work, we have

$$V = \sqrt{2E} \left[\frac{3}{5\frac{m}{c} + 2\left(\frac{m}{c}\right)\frac{R+r}{r} + \frac{2r}{R+r}} \right]^{1/2} \quad [11]$$

where V is the collapse velocity of the cylinder in the radial direction; E is the Gurney energy; m and c are the masses of metal and explosive charge, respectively; R is the external radius of the explosive charge (equal to 30 mm); and r is the external radius of the cylinder (equal to 15 mm). The Gurney energy was obtained through the empirical relationship by Kennedy:^[29]

$$\sqrt{2E} = D/3 \quad [12]$$

where D is the detonation velocity, equal to 4000 m/s. The collapse velocity was found to be equal to 520 m/s. Recent calculations using RAVEN^[23] have yielded a collapse velocity of 560 m/s. These calculations represent an upper bound and show that the measured value of 200 m/s for initial velocity is reasonable. Incorporation of the plastic deformation work reduces the calculated velocity.

To avoid extra wave reflection from the free interface between the stopper and the specimen, a shrink-fit technique was applied. The outer diameter of the stopper was designed to be 0.03-mm larger than the inner diameter of the specimen.

The collapse of thick-walled cylinder specimen occurs in a plane strain condition. The stress state can be considered as a superposition of a hydrostatic pressure and a pure

shear stress due to the axisymmetrical geometry and loading. While the radial stress is zero at the internal surface, the tangential stress is maximum. The shear stress is highest at the internal surface, and this is where shear localization starts. For single crystals, the symmetry of the process is broken because of anisotropy of plastic deformation, and the crystallographic differences manifest themselves through a distortion of the cylindrical shape.

The maximum shear strain occurs on the internal surface of the cylindrical specimen, and thus, shear bands preferentially initiate there. After each experiment, the cylinders were sectioned, ground, and polished. The lengths of shear bands, l_i , the edge displacements, δ_i , the average radius of final internal boundary, R_f , and the angle between spatial positions from origin, Ψ_i , were measured, as shown in Figure 4. In order to compare the deformation at the different positions on the specimen, an effective strain is used:

$$\epsilon_{ef} = \frac{2}{\sqrt{3}} \epsilon_{rr} = \frac{2}{\sqrt{3}} \ln \left(\frac{r_0}{r_f} \right) \quad [13]$$

where r_0 and r_f are the initial and final radii of a reference point, respectively. The effective global strain at the internal boundary of the specimen is considered as a characteristic value of deformation since all the specimens have the same initial dimensions. Based on the number of distinguishable shear bands, the average spacing between them is

$$L = \frac{\Psi_i R_f}{n_i \sqrt{2}} \quad [14]$$

where n_i is the number of shear bands at the particular region i and Ψ_i is the corresponding angle referring to the original

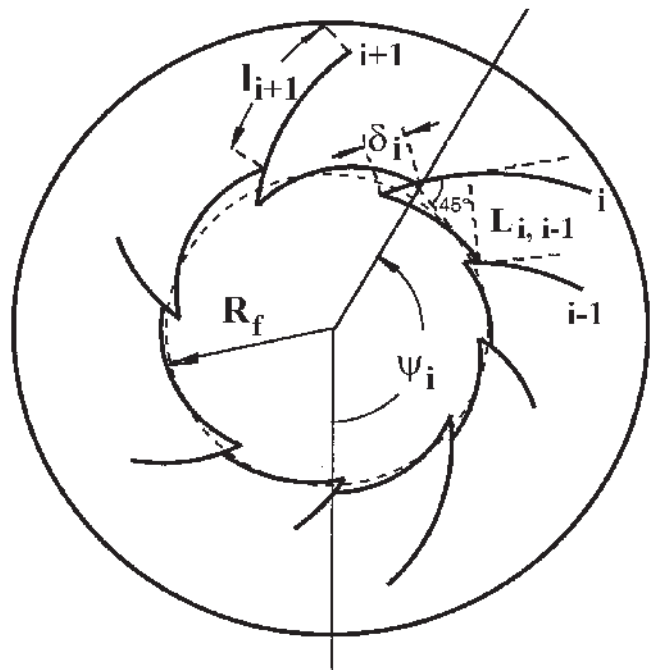


Fig. 4—Characteristics of shear-band pattern and basic measurement: Ψ_i is the reference angle and R_f is the final radius of the collapsed cylinder; and L_i is the spacing between the i th and the $i - 1$ th shear band, l_i is the length of the i th shear band, and δ_i is its edge length.

angle. If $n_i = n_{\text{total}}$, then $\Psi_i = 2\pi$. The spacing between shear bands decreases as plastic deformation proceeds due to the continuing deformation. The measured spacings are actually the sum of the real developing part and the geometrical part due to the change of the cylinder configuration. This geometrical effect needs to be subtracted from the results by an appropriate correction. The values of spacings at the initiation of the bands were taken as a reference. The spacing of shear bands can be expressed as

$$L = \frac{\Psi_i R_f}{n_i \sqrt{2}} \left(\frac{R_{f0}}{R_f} \right) \cong \frac{\sum_i L_{i,i-1}}{n_i} \left(\frac{R_{f0}}{R_f} \right) \quad [15]$$

where R_{f0} is the radius of the specimen at shear band initiation, R_f is the final radius at any larger effective strain, and $L_{i,i-1}$ is defined as the spacing between i th and $(i - 1)$ th shear bands in Figure 4. Since $R_f < R_{f0}$, the corrected spacing based on the final configuration always has a lower value.

III. RESULTS AND DISCUSSION

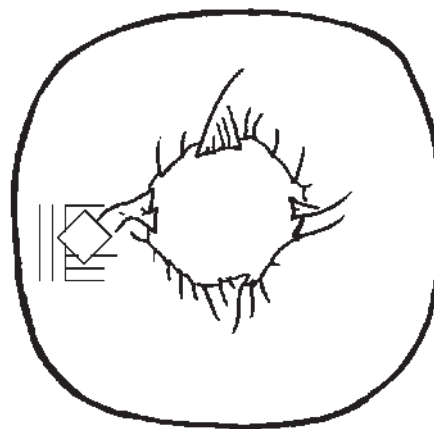
A. Mesoscopic Aspects

Figure 5 shows the differences in collapse geometry between monocrystalline Fe-15 pct Cr-15 pct Ni and polycrystalline AISI 304 stainless steel, which has a similar composition: Fe-18 pct Cr-8 pct Ni. The crystallographic anisotropy creates a mechanical anisotropy in the monocrystal. This results in a difference in resistance to the collapse. Figure 6 shows the stress-strain response obtained by Stone and Thomas^[16] for the [001] and [011] directions. The Fe-Cr-Ni monocrystal has a response characteristic of fcc monocrystals: the [001] orientation has four slip systems with identical Schmid factors and therefore a higher yield stress. Thus, the [001] direction shows a greater resistance to collapse. This symmetry is shown by the pronounced tendency of the cylinder to become square.

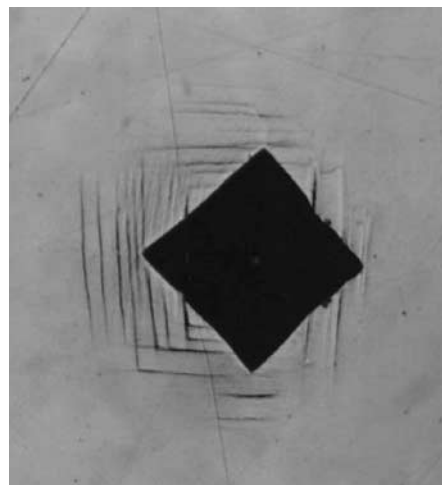
Figure 7 shows montages made from photomicrographs for the three testing conditions. Although all three conditions exhibit the effects of plastic anisotropy, this is most pronounced for the specimen imploded at ambient temperature in the austenitic condition. The ratios between the smallest and largest outside diameters are equal to 0.86, 0.94, and 0.96, respectively. The specimen imploded after martensitic transformation (Figure 7(c)) is the most symmetric. This is due to the formation of different martensite variants, providing a more isotropic plastic response.

The number of shear bands formed was also affected by the condition. The untransformed and pretransformed conditions showed a large number of shear bands (N_s equal to 41 and 56, respectively). These numbers are given in Figure 7. The condition transforming while deforming showed a marked decrease in the number of shear bands: $N_s = 10$. This drastic reduction is the direct result of the competition between shear localization and martensitic transformation as plastic deformation accommodation means.

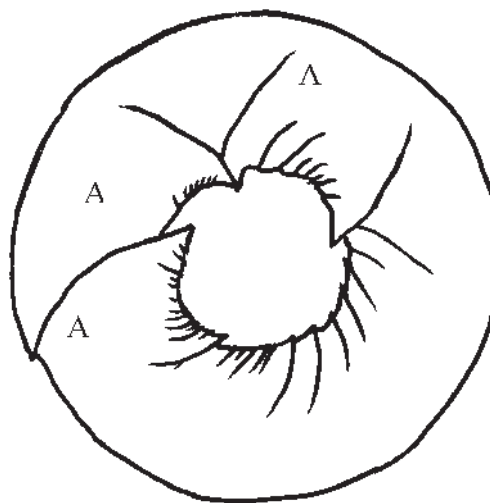
This drastic reduction in the number of shear bands and the associated increase in their spacing can be explained partially by the reduced yield stress. Both the Grady-Kipp^[30]



(a)



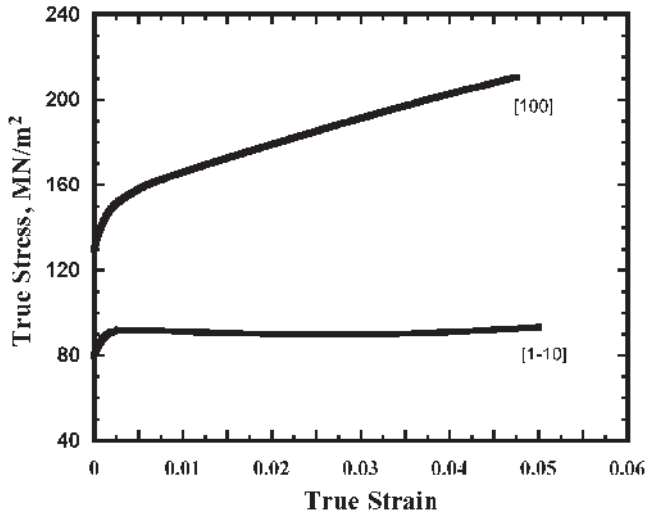
(b)



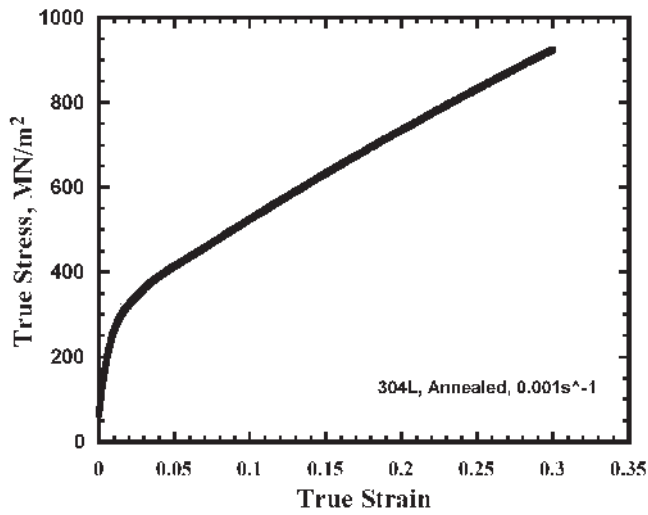
(c)

Fig. 5—Configuration of shear bands in specimen subjected to implosion to $\epsilon_{ef} = 0.92$: (a) in Fe-15Cr-15Ni monocrystal, cylinder axis: [100]; (b) microhardness indentation and traces of [111] slip planes (the traces are [110] orientation); and (c) polycrystalline Fe-18Cr-8 Ni.

and Wright-Ockendon-Molinari^[31,32] analyses predict an inverse relation between yield stress and shear-band spacing. The Grady-Kipp model is based on momentum diffusion



(a)



(b)

Fig. 6—(a) True stress–true strain curves for Fe-15 wt pct Ni-15 wt pct Cr monocrystal along [100] and [110] orientations (adapted from Stone and Thomas^[16]), (b) Quasi-static response of stainless steel 304L in annealed condition.

and is thought to describe the later stage of the shear localization,^[29] whereas the Wright–Ockendon–Molinari^[31,32] model is based on a perturbation analysis to explain the initial growth of shear bands at early stages. These predictive equations can be expressed as:

Grady–Kipp (GK):

$$L = 2\pi \left[\frac{kC}{\dot{\gamma}^3 a^2 \tau_0} \right]^{1/4} \cdot \frac{9^{1/4}}{\pi} \quad [16]$$

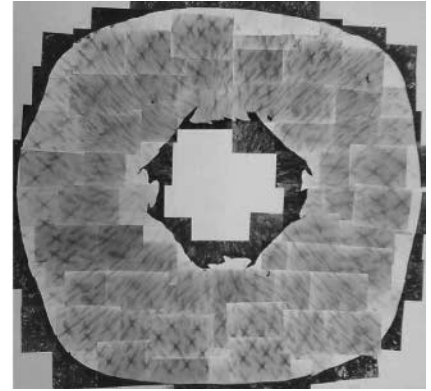
Wright–Ockendon (WO):

$$L = 2\pi \left[\frac{kC}{\dot{\gamma}^3 a^2 \tau_0} \right]^{1/4} \cdot m^{3/4} \quad [17]$$

$$D_{\min}/D_{\max}=0.86$$

$$L = 0.983 \text{ mm}$$

$$N_s=41$$

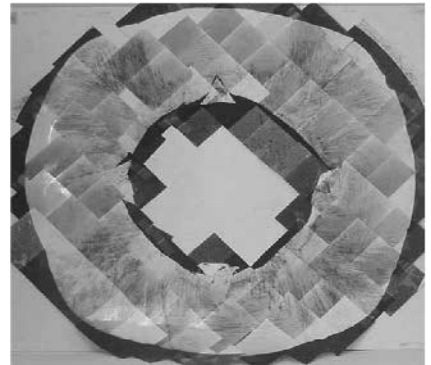


(a)

$$D_{\min}/D_{\max}=0.94$$

$$L = 4.03 \text{ mm}$$

$$N_s=10$$

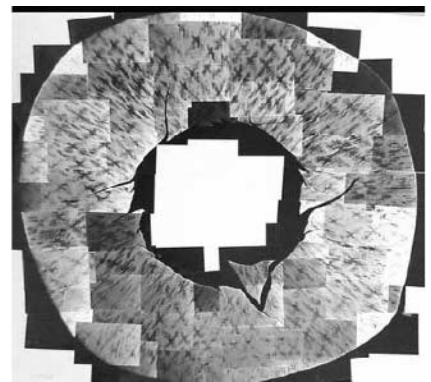


(b)

$$D_{\min}/D_{\max}=0.96$$

$$L = 0.72 \text{ mm}$$

$$N_s=56$$



(c)

Fig. 7—Montages showing deformation pattern and shear bands for specimens deformed under three regimes of deformation: (a) deformation at ambient temperature, no transformation; (b) deformation at 188 K, simultaneous transformation; and (c) deformation of pretransformed structure.

Molinari:

$$L = 2\pi \left[\frac{kC}{\dot{\gamma}^3 \tau_0 a^2} \right]^{1/4} \cdot \left[\frac{m^3(1 - aT_0)^2}{(1 + m)} \right]^{1/4} \quad \text{for } n = 0 \quad [18]$$

The three models have a dependence of yield stress that is fairly weak ($L \propto \tau_0^{-1/4}$). The WO and Molinari models are the same except for a factor $[(1 - aT_0)^2/(1 + m)]^{1/4}$. Since m is much less than 1 and T_0 is the reference temperature, this factor is approximated as $(1 - aT_0)^{1/2}$. The form of the

equations enables direct comparison between the three predictive models. Generally speaking, if the strain-hardening effect is ignored, the Molinari prediction is of the same order as the WO model, except for the coefficient. The coefficient in the GK model is independent of work hardening. The coefficient of the GK model is 0.55, which is at least 5 to 10 times larger than $m^{3/4}$ since m is about 10^{-2} for most metals.

These models predict, for instance, an increase in the spacing, L , by 50 pct if the yield stress is reduced by 80 pct. The experimental results are much more dramatic, as shown by the quantitative measurements in Figure 8. The spacing of shear bands was calculated assuming that they initiated at a strain of 0.1. The spacing in the condition undergoing simultaneous transformation ($L = 4.03$ mm) and deformation is

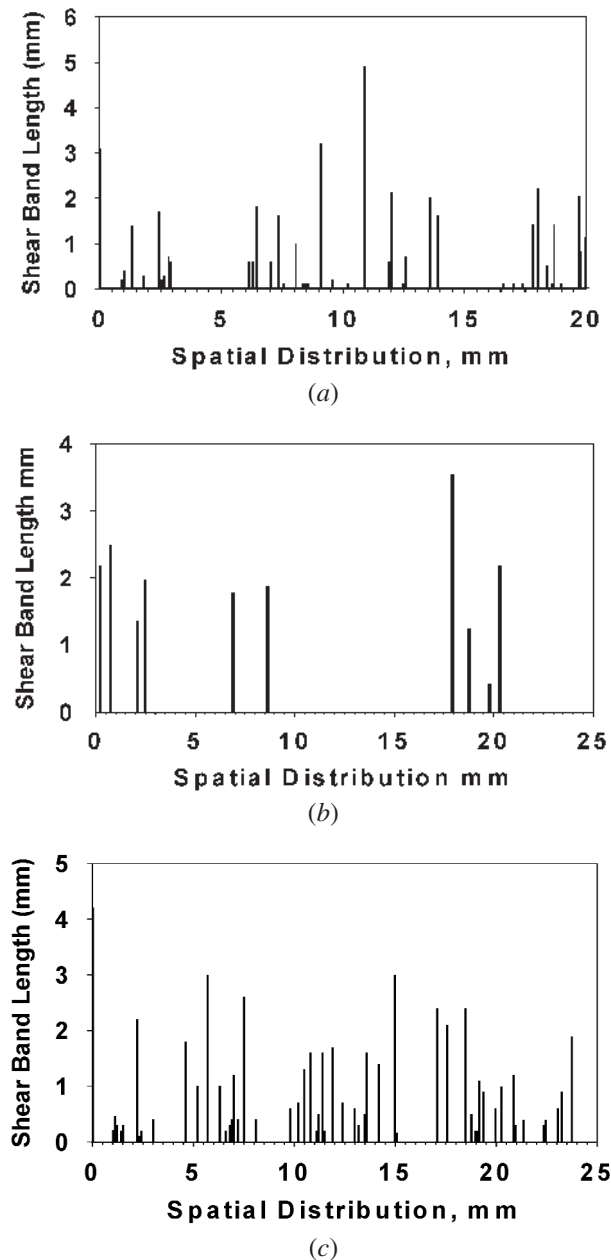


Fig. 8—Shear band distributions of the three specimens: (a) deformation at ambient temperature, no transformation; (b) deformation at 188 K simultaneous transformation; and (c) deformation of pretransformed structure.

4 times the spacing for the other conditions ($L = 0.98$ mm and $L = 0.72$ mm). This test was carried out at 188 K; the shear yield stress is reduced from 90 to 50 MPa. This corresponds to a 50 pct reduction in yield stress. Figure 9 shows the calculated shear-band spacings using the GK and WO analyses. It is clear that the spacing decreases as the yield stress increases. However, one does not obtain a fourfold increase in spacing for L . Thus, one has to look for another source for the difference: martensitic transformation competes with shear localization. This is explained in Section B. The anisotropic plastic deformation in copper monocrystals was modeled by Nemat-Nasser *et al.*^[33] The results presented herein are consistent with the simulations.

B. Microstructural Aspects

The close observation of the microstructure revealed features worth reporting. Figure 10 shows the austenitic material imploded at ambient temperature. The austenitic monocrystal had a pattern of gray regions forming “x”s. These regions are diffuse and indicate that the composition of the alloy is

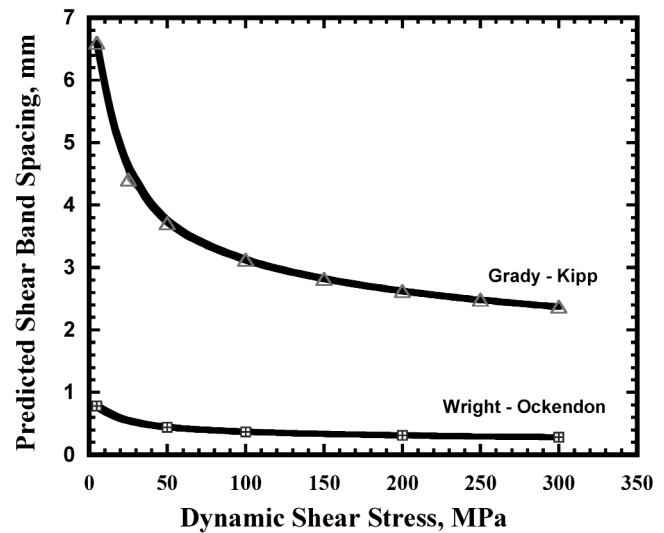


Fig. 9—Calculated shear-band spacing for Fe-Ni-Cr alloy as a function of the dynamic yield stress according to GK^[30] and WO^[31] theories.



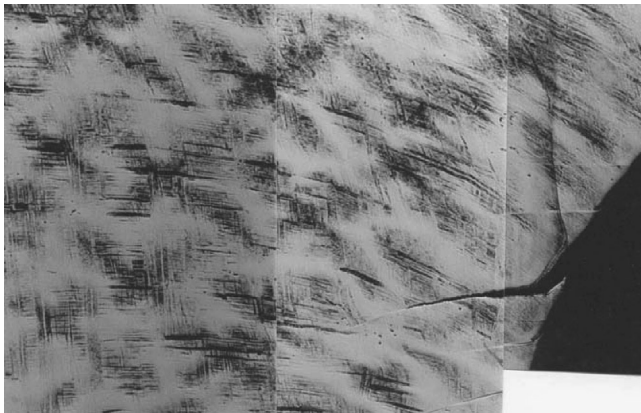
Fig. 10—Micrographs of shear bands formed by deformation without transformation: deformation at 300 K (gray × markings are the product of compositional fluctuations).

not entirely homogeneous. These fluctuations do not affect the response of the alloy but serve as markers. Three or four shear bands initiate in the inner surface of the sample.

The pretransformed material was cooled to 77 K and then reheated prior to implosion. The microstructure, shown in



(a)



(b)

Fig. 11—Pretransformed material was cooled to 77 K and then reheated prior to implosion: (a) region on outer edge of the imploded cylinder and (b) region on inner surface showing shear bands.

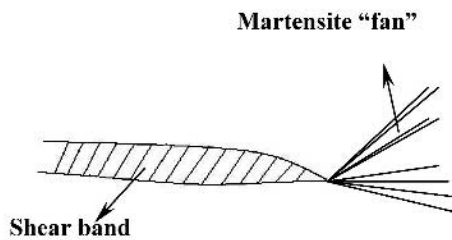
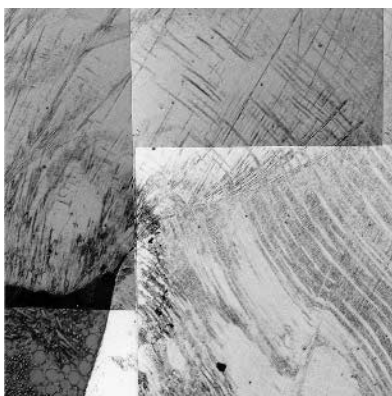
Figure 11(a), consists of martensite laths along the habit planes. This complex microstructure is much more isotropic than the initial monocrystalline austenite and exhibits a significantly higher yield stress; therefore, the spacing among shear bands is smaller. Figure 11(b) shows the shear bands cutting through the pre-existing martensite.

Figure 12 shows close-ups of the material imploded at 188 K; there is clear evidence of stress-assisted/strain-induced martensite as well as shear localization. Figure 12(a) shows one principal shear band and several martensite laths forming at its tip, in a fan-like pattern. A schematic is also shown, where one can see this phenomenon in a clearer manner. Figure 12(b) shows a region along the surface in which the plastic deformation was accommodated by transformation. Several laths can be seen, emanating from the surface. Accordingly, no shear bands were formed in this region.

Martensite laths do not evolve from shear band tips in all cases. There seems to be a requirement for orientation compatibility. It is proposed herein that martensite fans form at the tip of the shear band, when the martensite habit plane and shear direction are compatible with the shear imparted by the tip of the shear band. This is shown in schematic form in Figure 13.

One might envisage the formation of martensite within the shear bands, but such an event is highly unlikely. The temperature rise that results from plastic deformation is significant, and material is only expected to form within 20 to 30 K from M_s .

Transmission electron microscopy was conducted on the shear band. The features revealed are identical to the ones seen for a polycrystalline AISI 304 stainless steel. In general, an equiaxed structure with grains in the range of 100 to 300 nm was observed. This is shown in Figure 14(a). The formation of submicrometer grains has been attributed to a rotational dynamic recrystallization process.^[34] The selected area diffraction pattern shows the segmented ring characteristic of several micrograins simultaneously diffracting. The structure is very similar to the one produced by intense plastic deformation processes (ball milling, ECAP, torsion, etc). It is thought that the mechanism of formation of these structures with refined grain sizes is also similar.



(a)



(b)

Fig. 12—Martensite transformation during deformation (Fe-15Cr-15Ni collapsed cylinder at $T = 188$ K): (a) interaction of shear bands and stress-assisted martensite, and schematic of martensite fan; and (b) region along internal surface where deformation was accomplished by martensite transformation.

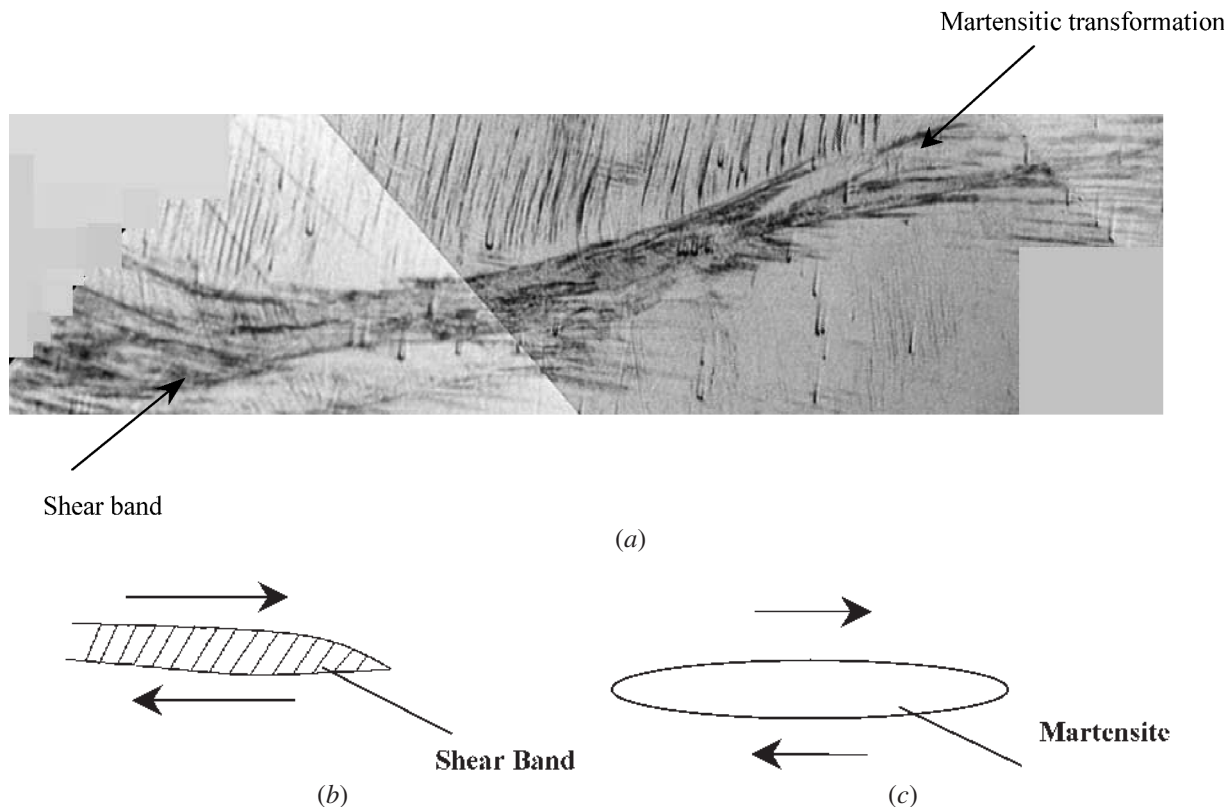


Fig. 13—(a) Shear bands and martensite interacting with each other, (b) Shear stresses around shear band. (c) Shear stresses around martensite.

Figure 14(a) also shows an amorphous region. This is confirmed by the diffraction pattern of Figure 14(b). The formation of the amorphous region is indeed a surprising finding. It is thought to be due to melting and very high rate resolidification. A similar microstructure was also seen by Meyers *et al.*^[34] for AISI stainless steel. Barbee *et al.*^[35] obtained the amorphous form by sputter depositing stainless steel. However, this was only possible for higher carbon concentrations. The cooling rate within the shear band is extremely high. This could possibly lead to resolidification in the glassy state from the melt. The martensitic structure was also identified by transmission electron microscopy. Figure 15 shows both bright- and dark-field images of what is presumed to be strain-induced martensite.

C. Computational Modeling

The anisotropic collapse process was modeled by RAVEN considering the widely different mechanical responses along $[1\bar{1}0]$ and $[100]$. A Johnson–Cook constitutive equation was used:^[38]

$$\sigma = (A + B\varepsilon^n) \left(1 + C \ln \frac{\dot{\varepsilon}}{\dot{\varepsilon}_0} \right) \left[1 - \left(\frac{T - T_r}{T_m - T_r} \right)^m \right] \quad [19]$$

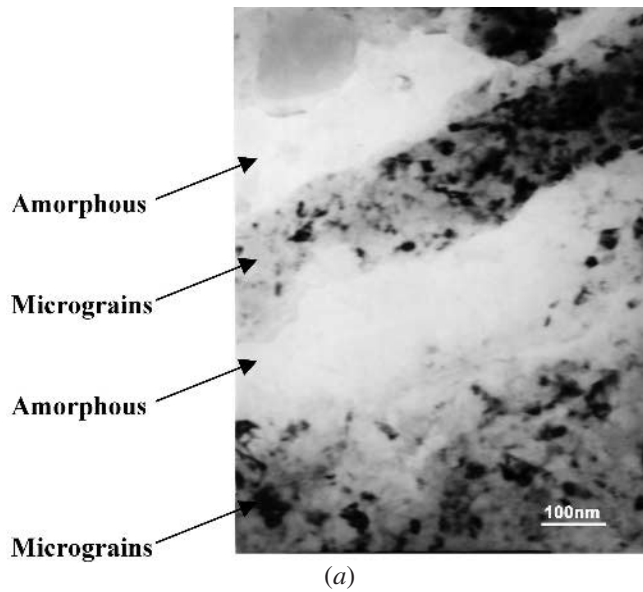
The parameters used in calculations are given in Table II. The RAVEN code^[39,40,41] was used, incorporating crystal elasto-viscoplasticity with the standard 12 $\{110\}\langle 111 \rangle$ slip systems. A Gruneisen equation of state is used to model the pressure response. In the Johnson–Cook model, elastic moduli are pressure dependent, and slip system strength

scales with the pressure-dependent moduli. Dislocation glide kinetics obey a power-law relationship between the resolved shear stress and the slip system shearing rate. The rate sensitivity in this relationship is temperature dependent.

For advection, the lattice orientation is stored as a quaternion. As noted, for example, averaging quaternion parameters produces a meaningful average lattice orientation and thus quaternions are a natural means of parameterizing and storing material orientation for advection. The elastic stretch is stored in the crystal lattice frame.

In the simulations, the material has a uniform initial lattice orientation, and the cube axes are aligned with the reference coordinate frame. Thus, only one quarter of the thick-walled cylinder needs to be modeled. The explosive is modeled using a pressure boundary condition with peak pressure of 5 GPa.^[41] Rise time is 2 ms and decay time is 6 ms.

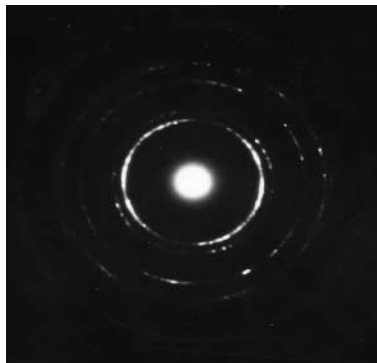
The evolution of plastic deformation for three plastic strains is shown in Figure 16. Figure 16(a) shows the initial configuration (quarter space). As the strain is increased, the deformation becomes increasingly anisotropic. The effective strains are given in different colors. As the collapse is completed, there are regions subjected to an effective strain equal to one. The softer directions ($\langle 011 \rangle$ and $\langle 01\bar{1} \rangle$) deform more and the harder direction ($\langle 010 \rangle$) undergoes less deformation. The final configuration for $\varepsilon_{\text{eff}} = 0.92$ is shown in Figure 17. The cross section becomes square in agreement with our experimental observation.^[36] This anisotropic plastic deformation is the same as the alloy collapsed at 298 K, where no martensitic transformation takes place. It should be noticed that the central hole deforms more heterogeneously than the external surface.



(a)

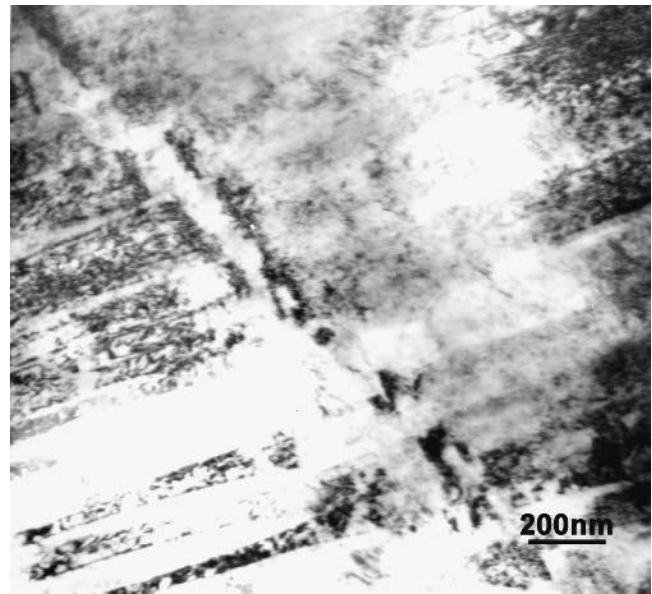


(b)

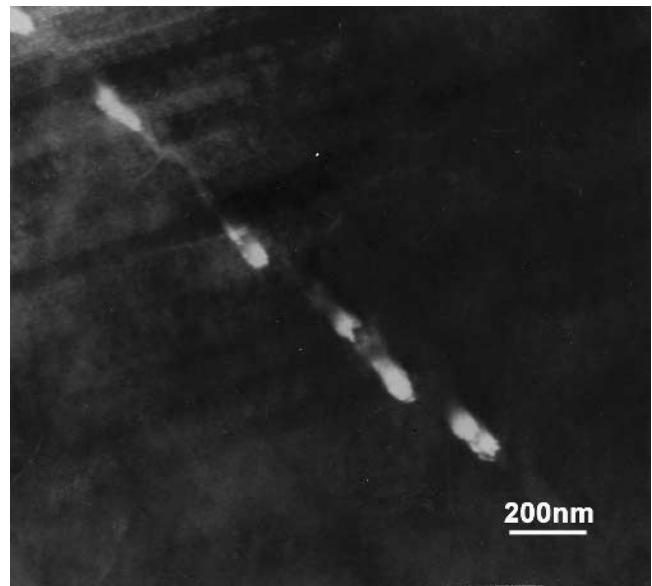


(c)

Fig. 14—(a) Transmission electron micrograph of shear band showing microcrystalline and amorphous regions. (b) Diffraction rings from the amorphous. (c) Diffraction rings from the microcrystalline zones.



(a)



(b)

Fig. 15— α' -martensite phase nucleation at the intersection between twins and bands: (a) bright field and (b) dark field.

Table II. Parameters for the Johnson–Cook Equation Used in Modeling Anisotropic Plastic Deformation of Fe-15Ni-15Cr Monocrystal

Orientation	A* (MPa)	B* (MPa)	C*	<i>m</i>	<i>n</i> **	$\dot{\epsilon}_0^{**}$ (s ⁻¹)	<i>T_r</i> (K)	<i>T_m</i> (K)
[1 $\bar{1}$ 0]	80	20	0.067	0.95	0.03	10 ⁻³	185	485
[100]	120	80	0.024	0.75	0.09	10 ⁻³	185	785

*Calculated by data from Stone and Thomas.^[16]

**From Xue et al. [23].

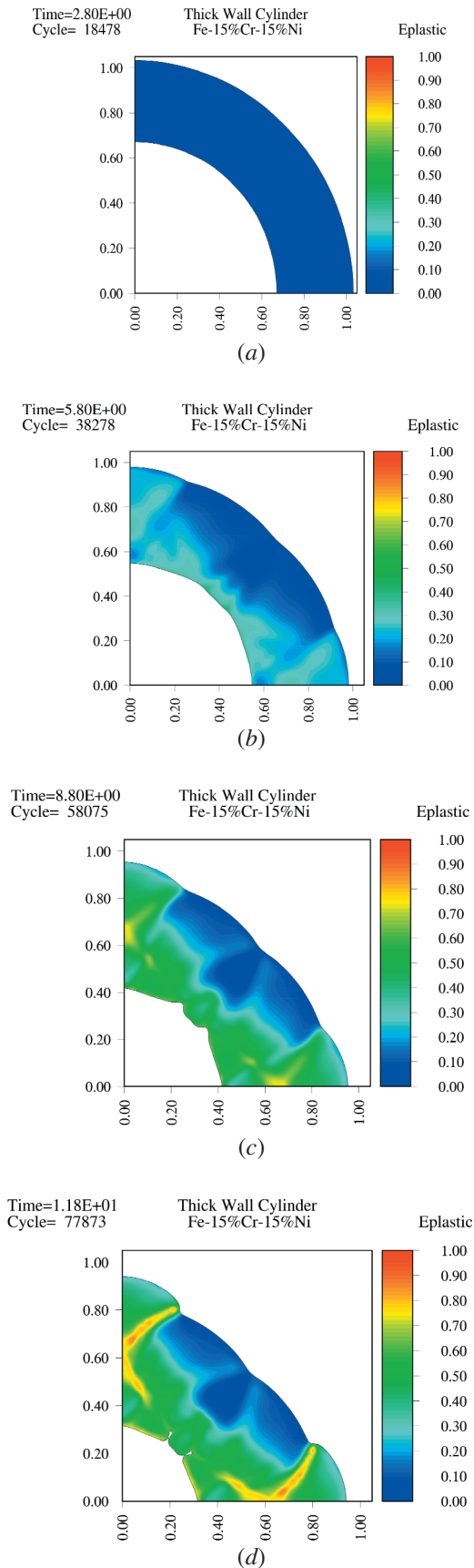


Fig. 16—RAVEN simulation of cylinder collapse driven by detonation: (a) initial cylindrical cross section; and (b) and (c) configuration at increasing plastic strains. Effective strains given in color scale.

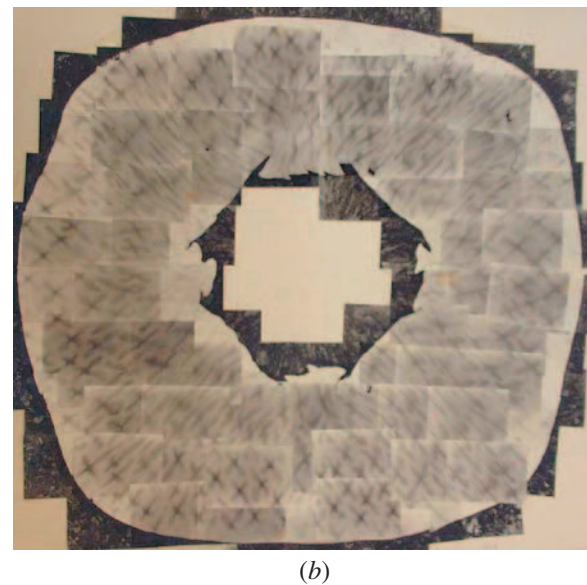
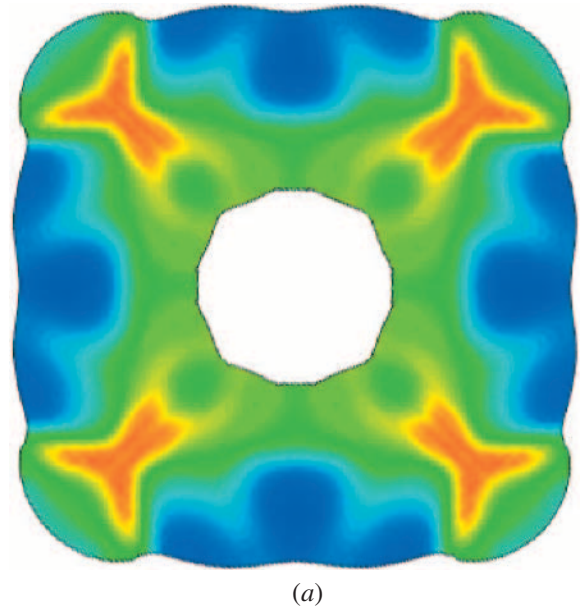


Fig. 17—(a) Final computed configuration for anisotropic collapse of single crystal. (b) Experimental observation for anisotropic collapse of single crystal.

IV. SUMMARY AND CONCLUSIONS

Monocrystalline Fe-15 wt pct Cr-15 wt pct Ni cylindrical specimens with 32-mm diameter were collapsed by the thick-walled cylinder implosion technique in three regions: $T < M_s$, $M_s < T < M_s^\sigma$, and $T > M_s^\sigma$.

1. The ratios between the smallest and largest outside diameters are equal to 0.96, 0.94, and 0.86 for the conditions $T < M_s$, $M_s < T < M_s^\sigma$, and $T > M_s^\sigma$, respectively. The specimen imploded after martensitic transformation is the most symmetric (0.96; $T < M_s$). The specimen imploded at 273 K, in the austenitic condition ($T > M_s^\sigma$; without transformation) exhibits the effects of plastic anisotropy most pronouncedly (0.86).

2. The number of shear bands formed was significantly affected by the condition. The nontransforming and pretransformed conditions showed a large number of shear bands (N_s equal to 41 and 56, respectively). The condition transforming while deforming showed a marked decrease in the number of shear bands: $N_s = 10$.
3. After implosion at 273 K, the austenitic monocrystal had a pattern of gray regions. These regions are diffuse and indicate that the composition of the alloy is not entirely homogeneous.
4. For the pretransformed material, which was cooled to 77 K and then reheated prior to implosion, the structure consists of martensite laths along the habit planes. This complex microstructure is much more isotropic than the initial monocrystalline austenite and exhibits a significantly higher yield stress curve; the spacing among shear bands is also smaller.
5. For the material imploded at 188 K, there is clear evidence for stress-assisted/strain-induced martensite as well as shear localization. Several laths can be seen, emanating from the surface. Accordingly, less shear bands were formed in this region. Some shear bands terminate in a martensite fan.
6. Calculated shear-band spacing compared favorably with prediction from the WO theory for the nontransforming condition ($L = 0.72$ and 0.98 mm). However, the condition transforming concurrently with deformation exhibited a much larger shear-band spacing ($L \sim 4$ mm), which cannot be accounted for by a yield stress decrease alone. Thus, it is proposed that martensitic transformation competes with shear localization and indeed decreases its incidence.
7. Transmission electron microscopy revealed a microcrystalline structure with equiaxed grains of 20 to 100 nm and, in some places, amorphous regions.
8. The results of the computational modeling predict an anisotropic collapse and are in agreement with experimental observations.

ACKNOWLEDGMENTS

We thank Dr. V. Usherenko, Minsk, for carrying out the implosion experiments. The support of B. Cao, by the Lawrence Livermore National Laboratory, is gratefully acknowledged. Dr. D. Lassila provided guidance throughout the investigation. Dr. Q. Xue provided valuable assistance in the initial stages of the investigation. We thank Professor G. Stone for generously providing us with the Fe-15 pct Ni-15 pct Gr monocrystals. He kept them for 30 years and then parted with them. We thank Dr. Nathan Barton and Mr. Franck Grignon for help in the simulations.

REFERENCES

1. D. Peirce, R.J. Asaro, and A. Needleman: *Acta Metall.*, 1983, vol. 31, pp. 1951-76.
2. C.J. Shih, M.A. Meyers, and V.F. Nesterenko: *Acta Mater.*, 1998, vol. 11, pp. 4037-65.
3. C.J. Shih, V.F. Nesterenko, and M.A. Meyers: *J. Appl. Phys.*, 1998, vol. 83, pp. 4660-71.
4. M.A. Meyers: *Encyclopedia of Materials: Science and Technology*, Elsevier, New York, NY, 2001, pp. 7093-103.
5. V.F. Nesterenko, M.A. Meyers, and H.C. Chen: *Acta Mater.*, 1996, vol. 44, pp. 2017-26.
6. V.F. Nesterenko: *Dynamics of Heterogeneous Materials*, Springer-Verlag, New York, NY, 2001.
7. J.W. Rudnicki and J.R. Rice: *J. Mech. Phys. Solids*, 1975, vol. 23, pp. 371-94.
8. H.C. Rogers: *Ann. Rev. Mater. Sci.* 1979, vol. 2, pp. 283-311.
9. R.W. Armstrong, R. Batra, M.A. Meyers, and T.W. Wright: *Mech. Mater.*, 1994, vol. 17, pp. 83-328.
10. Y. Bai and B. Dodd: *Adiabatic Shear Localization*, Pergamon, Oxford, United Kingdom, 1992.
11. M.A. Meyers: *Dynamic Behavior of Materials*, Wiley, New York, NY, 1994.
12. T.W. Wright: *The Physics and Mathematics of Adiabatic Shear Bands*, Cambridge University Press, Cambridge, United Kingdom, 2002.
13. V.F. Nesterenko, M.A. Meyers, H.C. Chen, and J.C. LaSalvia: *Appl. Phys. Lett.*, 1994, vol. 65, pp. 3069-71.
14. V.F. Nesterenko, M.A. Meyers, J.C. LaSalvia, M.P. Bondar, Y.J. Chen, and Y.L. Lukyanov: *Mater. Sci. Eng. A*, 1997, vol. 229, pp. 23-41.
15. V.F. Nesterenko, M.A. Meyers, and T.W. Wright: *Acta Mater.*, 1998, vol. 46, pp. 327-40.
16. G. Stone and G. Thomas: *Metall. Trans.*, 1974, vol. 5, pp. 2095-2102.
17. J.R.C. Guimaraes, J.C. Gomes, and M.A. Meyers: *Proc. 1st JIM Int. Symp.*, Kobe, Japan, May 1976, *Suppl. Trans. JIM*, 1976, vol. 17, pp. 411-17.
18. J.R. Patel and M. Cohen: *Acta Metall.*, 1953, vol. 1, pp. 531-38.
19. J.D. Eshelby: *Proc. R. Soc.*, 1957, vol. A241, pp. 376-95.
20. J.D. Eshelby: *Proc. R. Soc.*, 1959, vol. A252, pp. 561-69.
21. T. Mura: *Micromechanics of Solids*, Martinus Nijhoff, The Hague, 1982.
22. L. Kaufman and M. Cohen: *Progr. Met. Phys.*, 1958, vol. 7, pp. 165-200.
23. Q. Xue, V.F. Nesterenko, and M.A. Meyers: *Int. J. Impact Eng.*, 2003, vol. 28, pp. 257-80.
24. V.F. Nesterenko and M.P. Bondar: *DYMAT J.*, 1994, vol. 1, p. 245.
25. D.A. Shockey: in *Metallurgical Applications of Shock-Wave and High-Strain-Rate Phenomena*, L.E. Murr, K.P. Staudhammer, and M.A. Meyers, eds., 1986, pp. 633-56.
26. V.F. Nesterenko, M.A. Meyers, and T.W. Wright: *Metallurgical and Materials Applications of Shock-Wave and High-Strain-Rate Phenomena*, L.E. Murr, K.P. Staudhammer, and M.A. Meyers, eds., Elsevier Science, Oxford, United Kingdom, 1995, pp. 397-404.
27. V.F. Nesterenko, M.P. Bondar, and I.V. Ershov: *High-Pressure Science and Technology*, AIP Conf. Proc., 1993, S.C. Schmidt, ed., AIP Press, New York, NY, 1994, vol. 309, p. 1173.
28. M.A. Meyers and S.L. Wang: *Acta Metall.*, 1988, vol. 36, pp. 925-36.
29. J.E. Kennedy: *Behavior and Utilization of Explosives in Engineering Design*, 12th Ann. Symp., ASME, Albuquerque, NM, 1972.
30. D.E. Grady and M.E. Kipp: *J. Mech. Phys. Solids*, 1987, vol. 35, pp. 95-119.
31. T.W. Wright and H. Ockendon: *Int. J. Plasticity*, 1996, vol. 12, pp. 927-34.
32. A. Molinari: *J. Mech. Phys. Solids*, 1997, vol. 45, pp. 1551-75.
33. S. Nemat-Nasser, T. Okinada, V. F. Nesterenko, and M. Liu: *Phil. Mag.*, 1998, vol. 78, pp. 1151-74.
34. M.A. Meyers, Y.B. Xu, Q. Xue, M.T. Perez-Prado, and T.R. McNelley: *Acta Mater.*, 2003, vol. 51, pp. 1307-25.
35. T.J. Barbee, B.E. Jacobsen, and D.L. Keith: *Thin Solid Films*, 1979, vol. 63, pp. 143-50.
36. B.Y. Cao, M.A. Meyers, V.F. Nesterenko, D. Benson, and Y.B. Xu: *13th Am. Physical Society Topical Conf. on Shock Compression of Condensed Matter*, 2003.
37. G.R. Johnson and W.H. Cook: Paper presented at the *7th Int. Symp. on Ballistics*, The Hague, 1983.
38. D.J. Benson: *RAVEN: User's Manual ver 2000*.
39. D.J. Benson: *Comp. Meth. Appl. Mech. Eng.*, 1992, vol. 99, p. 235.
40. M.A. Meyers, D.J. Benson, and E.A. Olevsky: *Acta Mater.*, 1999, vol. 47 (7), pp. 2089-2108.
41. B.M. Dobratz: *Explosives Handbook: Properties of Chemical Explosives and Explosives Simulants*. UCRL-52997, Livermore National Laboratory, Livermore, CA, 1981.